

Geophysical Research Letters

RESEARCH LETTER

10.1029/2019GL083180

Key Points:

- The new model can reproduce observations beyond MHD including dawn-dusk asymmetries in Mercury's magnetotail and field-aligned currents
- The new model is essential for capturing the electron physics associated with collisionless magnetic reconnection in Mercury's magnetosphere
- The induction response arising from the electromagnetically coupled interior plays an important role in solar wind-Mercury interaction

Correspondence to:

C. Dong,
dcfy@princeton.edu

Citation:

Dong, C., Wang, L., Hakim, A., Bhattacharjee, A., Slavin, J. A., DiBraccio, G. A. & Germaschewski, K. (2019). Global ten-moment multifluid simulations of the solar wind interaction with Mercury: From the planetary conducting core to the dynamic magnetosphere. *Geophysical Research Letters*, 46, 11,584–11,596. <https://doi.org/10.1029/2019GL083180>

Received 6 APR 2019

Accepted 20 SEP 2019

Accepted article online 15 OCT 2019

Published online 3 NOV 2019

Global Ten-Moment Multifluid Simulations of the Solar Wind Interaction with Mercury: From the Planetary Conducting Core to the Dynamic Magnetosphere

Chuanfei Dong^{1,2} , Liang Wang^{1,2} , Ammar Hakim² , Amitava Bhattacharjee^{1,2} , James A. Slavin³ , Gina A. DiBraccio⁴ , and Kai Germaschewski⁵ 

¹Department of Astrophysical Sciences, Princeton University, Princeton, NJ, USA, ²Princeton Center for Heliophysics, Princeton Plasma Physics Laboratory, Princeton University, Princeton, NJ, USA, ³Department of Climate and Space Sciences and Engineering, University of Michigan, Ann Arbor, MI, USA, ⁴NASA Goddard Space Flight Center, Greenbelt, MD, USA, ⁵Space Science Center and Physics Department, University of New Hampshire, Durham, NH, USA

Abstract For the first time, we explore the tightly coupled interior-magnetosphere system of Mercury by employing a three-dimensional ten-moment multifluid model. This novel fluid model incorporates the nonideal effects including the Hall effect, electron inertia, and tensorial pressures that are critical for collisionless magnetic reconnection; therefore, it is particularly well suited for investigating *collisionless* magnetic reconnection in Mercury's magnetotail and at the planet's magnetopause. The model is able to reproduce the observed magnetic field vectors, field-aligned currents, and cross-tail current sheet asymmetry (beyond magnetohydrodynamic approach), and the simulation results are in good agreement with spacecraft observations. We also study the magnetospheric response of Mercury to a hypothetical extreme event with an enhanced solar wind dynamic pressure, which demonstrates the significance of induction effects resulting from the electromagnetically coupled interior. More interestingly, plasmoids (or flux ropes) are formed in Mercury's magnetotail during the event, indicating the highly dynamic nature of Mercury's magnetosphere.

1. Introduction

Mercury, the closest planet to the Sun, is the only terrestrial planet other than Earth that possesses an intrinsic global magnetic field (Ness et al., 1974, 1975). The recent M_Ercury S_Urface, S_Pace E_Nvironment, G_Eochemistry, and R_Anging (MESSENGER) mission to Mercury presented us with the first opportunity to explore this planet's magnetosphere in great detail since the brief flybys of Mariner 10 (e.g., Slavin et al., 2007; Solomon et al., 2007). Many Earth-like magnetospheric features were observed at Mercury, including, but not limited to, magnetopause reconnection (DiBraccio et al., 2013; Slavin et al., 2009), the concomitant flux transfer events (Slavin et al., 2012) and cusp plasma filaments (Poh et al., 2016; Slavin et al., 2014), magnetotail flux ropes or plasmoids (DiBraccio et al., 2015), substorm processes including tail loading-unloading (Imber & Slavin, 2017), plasma wave activities (Sun et al., 2015), dipolarization fronts (Sundberg et al., 2012) and the associated electron acceleration (Dewey et al., 2017), cross-tail current sheet asymmetry and substorm current wedge formation (Poh et al., 2017), field-aligned currents (Anderson et al., 2014), and Kelvin-Helmholtz vortices (Gershman et al., 2015; Liljeblad et al., 2014; Sundberg et al., 2010).

According to MESSENGER observations, Mercury's dipole moment is much weaker than that of Earth, only 195 nT R_M^3 (where R_M is Mercury's radius, 2,440 km), and is offset in the northward direction by 484 ± 11 km or $\approx 0.2 R_M$ (Anderson et al., 2011). Later, those values were slightly modified in Anderson et al. (2012). Due to the relatively weak intrinsic planetary magnetic moment and the most extreme solar wind driving forces in the solar system, Mercury has a small but extremely dynamic magnetosphere whose size is about 5% that of Earth's magnetosphere (Winslow et al., 2013). More interestingly, Mercury has a large electrically conductive iron core with a radius of $\approx 0.8 R_M$ (Hauck et al., 2013; Smith et al., 2012). A unique aspect of Mercury's interaction system is that the large conducting core can induce observable magnetic fields in Mercury's magnetosphere (Johnson et al., 2016; Slavin et al., 2014; Zhong et al., 2015). It is worth noting that Hood and Schubert (1979) and Grosser et al. (2004) made some early quantitative estimates of the induction effect at Mercury. The core-induced magnetic fields have been demonstrated to play an important role in Mercury's

global solar wind interaction, especially during extreme space weather events (Jia et al., 2015; Heyner et al., 2016; Slavin et al., 2014, 2019). While the induction response generates additional magnetic flux that may protect Mercury from solar wind erosion, magnetic reconnection between the interplanetary magnetic field (IMF) and the planetary field removes magnetic flux from the dayside magnetopause and enables transfer of energy and momentum to the planetary inner magnetosphere, which consequently leads to the direct entry of solar wind plasma into the system. The magnetic flux transferred to the nightside magnetosphere may immediately undergo reconnection or be stored and later returned to the dayside during an intense episode of reconnection in the tail (Slavin et al., 2014). Magnetotail reconnection is also the dominant plasma process that transfers energy and momentum into Mercury's inner tail region by converting stored magnetic energy in the tail lobe into plasma kinetic energy in the plasma sheet. Magnetic reconnection, therefore, plays a crucial role in manipulating the magnetospheric dynamics of Mercury and other planets in our solar system and beyond.

Despite the significant achievements accomplished by direct spacecraft observations, in situ measurements are often taken at limited points along the trajectories of orbits or flybys. Such limitations, however, can be alleviated by numerical simulations, which allow the interpretation of in situ measurements in a three-dimensional context and distinguishing temporal from spatial fluctuations as well. Thus, numerical models, combined with in situ data, are the key for providing a global description of solar wind-planet interaction. In recent years, our understanding of terrestrial bodies has been significantly advanced by increasingly sophisticated numerical models. A large number of global models based on either fluid or hybrid (kinetic ion particles and massless electron fluid) approach have been developed for both magnetized planets such as Mercury (e.g., Exner et al., 2018; Jia et al., 2015; Kabin et al., 2008; Kidder et al., 2008; Müller et al., 2012; Richer et al., 2012; Trávníček et al., 2010) and unmagnetized planets such as Mars (Dong et al., 2014, 2015, 2018a, 2018b; Ledvina et al., 2017; Ma et al., 2014; Modolo et al., 2016) as well as exoplanets (Johansson et al., 2011; Dong et al., 2017a, 2017b, 2018c, 2019). However, none of these global models can accurately treat collisionless magnetic reconnection due to their lack of detailed electron physics. In order to solve this issue with affordable computational costs, two broad approaches have been proposed. Tóth et al. (2016) studied Ganymede's magnetosphere by employing a Hall magnetohydrodynamic model with embedded particle-in-cell boxes (MHD-EPIC) such that they can capture the collisionless reconnection physics in prescribed local regions. Meanwhile, Wang et al. (2018) developed a novel ten-moment multifluid model to study Ganymede's magnetosphere. Other than relying on the prescribed local particle-in-cell (PIC) boxes, the new global multimoment multifluid model incorporating the higher-order moments is capable of reproducing some critical aspects of the reconnection physics from PIC simulations (Ng et al., 2015, 2017, 2018; Wang et al., 2015).

Until now, no such approach (i.e., either MHD-EPIC or the multimoment multifluid approach) has been applied to study Mercury. This work will, therefore, be the first study of Mercury's dynamic magnetosphere using a ten-moment multifluid model. In order to capture the induction effects arising from the interior-magnetosphere electromagnetic coupling, we also implemented a resistive mantle and an electrically conductive core inside Mercury in this new model. This paper is structured as follows. In section 2, the ten-moment multifluid model and the model setup for Mercury are described. In section 3, we first validate the model through data-model comparison with MESSENGER data and then discuss the model results. We also conduct a hypothetical extreme event case study to demonstrate the significance of the induction effects. The conclusion is given in section 4.

2. Ten-Moment Multifluid Model for Mercury

2.1. Ten-Moment Equations

In this section, we briefly introduce the ten-moment multifluid model for Mercury within the GKEYLL framework (gkeyll.rfd.io). The ten moments refer to mass density mn , momentum mnu_x , mnu_y , mnu_z , and pressure tensor P_{xx} , P_{xy} , P_{xz} , P_{yy} , P_{yz} , P_{zz} . Conceptually, the ten-moment model is akin to a fluid version of PIC code, truncated at a certain order of moment, that is, second-order moment, the pressure. For Mercury, we solve ten-moment equations for both protons and electrons. It is noteworthy that the ten-moment model has been employed to study magnetic reconnection in multispecies plasmas including O^+ , H^+ , and e^- (Dong et al., 2016). The ten-moment equations for each species are given as follows:

$$\frac{\partial (m_s n_s)}{\partial t} + \frac{\partial (m_s n_s u_{i,s})}{\partial x_i} = 0, \quad (1)$$

$$\frac{\partial (m_s n_s u_{i,s})}{\partial t} + \frac{\partial \mathcal{P}_{ij,s}}{\partial x_j} = n_s q_s (E_i + \epsilon_{ijk} u_{j,s} B_k), \quad (2)$$

$$\frac{\partial \mathcal{P}_{ij,s}}{\partial t} + \frac{\partial Q_{ijk,s}}{\partial x_k} = n_s q_s u_{[i,s} E_{j]} + \frac{q_s}{m_s} \epsilon_{[ikl} \mathcal{P}_{k,j,s]} B_l, \quad (3)$$

where q is the charge and E and B are electric field and magnetic field, respectively. The subscripts $s = e, i$ represent the electron and ion species. It will be neglected hereinafter for convenience. The square brackets in equation (3) surrounding the indices represent the minimal sum over permutations of free indices needed to yield completely symmetric tensors. The first-order moment is defined as $mn u_i \equiv m \int f v_i d\mathbf{v}$, where f is the phase space distribution function and m and v_i denote the individual particle mass and velocity, respectively. Similarly, the second-order moment, \mathcal{P}_{ij} , and the third-order moment, Q_{ijk} , are defined as

$$\begin{aligned} \mathcal{P}_{ij} &= m \int f v_i v_j d\mathbf{v} \\ &= m \int f (v_i - u_i) (v_j - u_j) d\mathbf{v} + nm u_i u_j \\ &= P_{ij} + nm u_i u_j, \end{aligned} \quad (4)$$

and

$$\begin{aligned} Q_{ijk} &= m \int f v_i v_j v_k d\mathbf{v} \\ &= m \int f (v_i - u_i) (v_j - u_j) (v_k - u_k) d\mathbf{v} + u_{[i} \mathcal{P}_{jk]} - 2nm u_i u_j u_k \\ &= Q_{ijk} + u_{[i} \mathcal{P}_{jk]} - 2nm u_i u_j u_k, \end{aligned} \quad (5)$$

where P_{ij} is the pressure tensor and Q_{ijk} is the heat flux tensor. One of the key issues for a multimoment multifluid model is the closure problem, that is, how to close the equation systems and incorporate kinetic effects into a fluid framework, which is still an active research topic in fluid dynamics and plasma physics (Hunana et al., 2018). In this work, we adopt the following 3-D closure simplified by Wang et al. (2015) based on Landau-fluid closures (e.g., Hammett & Perkins, 1990):

$$\partial_m Q_{ijm} \approx v_t |k| (P_{ij} - p \delta_{ij}), \quad (6)$$

where v_t refers to the local thermal speed, p is the scalar pressure, and k is a free parameter that effectively allows for deviations from isotropy at length scales less than $1/|k|$. For *collisionless* magnetic reconnection, k should be a function of d_e given that *collisionless* magnetic reconnection takes place on the length scale of electron inertial lengths, d_e . Following the work of Wang et al. (2018), we define $k_s(\mathbf{x}, t)$ as $10/d_s(\mathbf{x}, t)$, where $d_s(\mathbf{x}, t)$ is the local inertial length of species s as a function of \mathbf{x} and t , such that it can provide a more accurate heat flux approximation because the species inertial length for the Mercury system can vary greatly in space. Interestingly, such closure can well reproduce the *collisionless* reconnection physics from a fully kinetic PIC code as shown in Wang et al. (2015).

The electromagnetic field is solved by full Maxwell equations

$$\frac{1}{c^2} \frac{\partial \mathbf{E}}{\partial t} = \nabla \times \mathbf{B} - \mu_0 \mathbf{J}, \quad (7)$$

$$\frac{\partial \mathbf{B}}{\partial t} = -\nabla \times \mathbf{E}, \quad (8)$$

where \mathbf{J} is the electric current density. Inside the planet interior $\mathbf{J} = \sigma \mathbf{E}$, where plasma convection, \mathbf{u} , can be neglected. Unlike the traditional magnetohydrodynamic (MHD) or hybrid models that solve the electric field \mathbf{E} by Ohm's law, here we update \mathbf{E} directly through the Ampere's law, equation (7). Therefore, electromagnetic waves are fully supported, similar to a PIC code. In order to demonstrate how a ten-moment model supports the reconnection electric field in *collisionless* magnetospheres, we rearrange equation (2) and obtain the following generalized Ohm's law (e.g., Lingam et al., 2017; Wang et al., 2015):

$$\mathbf{E} + \mathbf{v} \times \mathbf{B} = \underbrace{\eta \mathbf{J}}_0 + \frac{\mathbf{J} \times \mathbf{B}}{n|e|} - \frac{\nabla \cdot \mathbf{P}_e}{n|e|} + \frac{m_e}{n|e|^2} \left[\frac{\partial \mathbf{J}}{\partial t} + \nabla \cdot \left(\mathbf{v} \mathbf{J} + \mathbf{J} \mathbf{v} - \frac{\mathbf{J} \mathbf{J}}{n|e|} \right) \right]. \quad (9)$$

It should be noted that the Ohm's law formulated above is not numerically solved in the model.

In the case of 2-D antiparallel magnetic reconnection without a guide field, $\mathbf{B} = 0$ (hence $\mathbf{v} \times \mathbf{B} = 0$ and $\mathbf{J} \times \mathbf{B} = 0$) at reconnection sites or X-points; therefore, the divergence of the electron pressure tensor and the total derivative of the electric current are the primary sources of the reconnection electric field in a *collisionless* ($\eta = 0$) system (see equation (9) or Zweibel & Yamada, 2009). It is further demonstrated by PIC simulations that the reconnection electric field, E_z , is largely supported by the divergence of the off-diagonal elements of P_e , that is, $E_z = -(\partial_x P_{xz,e} + \partial_y P_{yz,e})/n_e|e|$, while traditional MHD and hybrid models only assume a scalar pressure, which does not contribute to E_z at reconnection sites (Wang et al., 2015). Even if a guide field exists, one can still get the similar conclusion. The multimoment multifluid code has been used to study many laboratory and space plasma physics problems (e.g., Ng et al., 2015, 2019; TenBarge et al., 2019; Wang et al., 2018). The details concerning the numerics and benchmark examples have been described in Hakim et al. (2006), Hakim (2008), and Wang et al. (2019).

2.2. Model Setup for Mercury

In a ten-moment model, the time step is mainly restricted by the speed of light. For this reason, we relax this restriction by using an artificially reduced speed of light, $c = 3,000$ km/s. We also apply a reduced ion-electron mass ratio $m_i/m_e = 25$ as the previous study (Wang et al., 2018), which is sufficiently large to separate the electron and ion scales. The upstream ion inertial length is set to $d_{i,in} = 0.05R_M$ and electron inertial length $d_{e,in} = 0.01R_M$. We adopt the Mercury-Solar-Orbital (MSO) coordinates, where the x axis points from Mercury toward the Sun, the z axis is perpendicular to planet's orbital plane, and the y axis completes the right-hand system. The computational domain is defined by $-15R_M \leq x \leq 5R_M$, $-30R_M \leq y, z \leq 30R_M$ with a nonuniform stretched Cartesian grid. The smallest grid size is $0.01 R_M$, and in turn, five cells are employed to resolve the ion inertial length and one cell for the electron inertial length. In order to capture the magnetospheric physics with minimum influences from numerical resistivity, we use a total of $\sim 4 \times 10^9$ cells such that we are able to cover most of the Hermean magnetosphere with the finest grid mesh (i.e., $0.01R_M$ resolution).

We implement Mercury's intrinsic dipole magnetic field B_0 with an equatorial surface strength of 195 nT and centered at $(0, 0, 0.2) R_M$ in MSO. The dipole field is prescribed and fixed in time. The total magnetic field \mathbf{B} equals $B_0 + B_1$, and we only solve the perturbation magnetic field, B_1 , in the model. The inner boundary for electromagnetic fields is set at core surface ($0.8 R_M$) where the conducting wall boundary conditions are applied. For plasma fluids, the inner boundary is set at the planet's surface, such that fluid moment equations are not solved inside the planet. If the surface plasma flow has an inflow component (i.e., $\mathbf{u} \cdot \mathbf{r} < 0$), absorbing boundary conditions are applied. If the surface plasma flow has an outflow component (i.e., $\mathbf{u} \cdot \mathbf{r} > 0$), we set the radial velocity equal to zero, and the plasma density and pressure are fixed at 1 cm^{-3} and 0.001 nPa , respectively (Jia et al., 2015). Outer boundary conditions are inflow at $x = 5R_M$ and float at the flanks and tail side.

3. Results and Discussion

In this section, we first validate the model through data-model comparison. We then discuss the model results including dayside and nightside magnetic reconnection, field-aligned currents, and cross-tail current sheet asymmetry. Finally, we present Mercury's magnetospheric response to a hypothetical extreme event.

3.1. Model Validation Through Data-Model Comparison

When magnetic reconnection occurs at the dayside magnetopause, it leads to an efficient transfer of energy and flux from the solar wind into the magnetosphere, which ultimately drives reconnection in the magnetotail. We choose to study MESSENGER's second flyby on 6 October 2018 (hereinafter referred to as M2), during which the IMF had a southward (negative B_z) component. For M2, the solar wind parameters are as follows: solar wind density, 40 cm^{-3} ; solar wind velocity in MSO, $\mathbf{u} = (-400, 50, 0) \text{ km/s}$; solar wind temperature, 18 eV; and IMF in MSO, $\mathbf{B}_{\text{IMF}} = (-15.2, 8.4, -8.5) \text{ nT}$, where the y -component of the solar wind flow velocity results from Mercury's orbital motion (Jia et al., 2015).

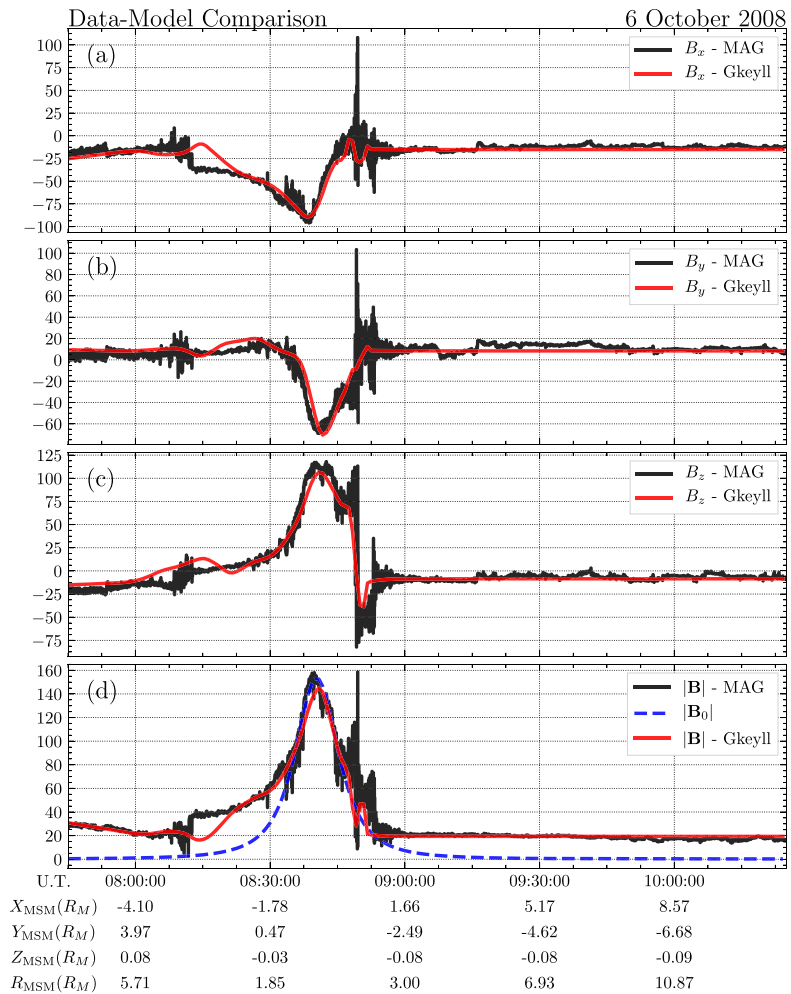
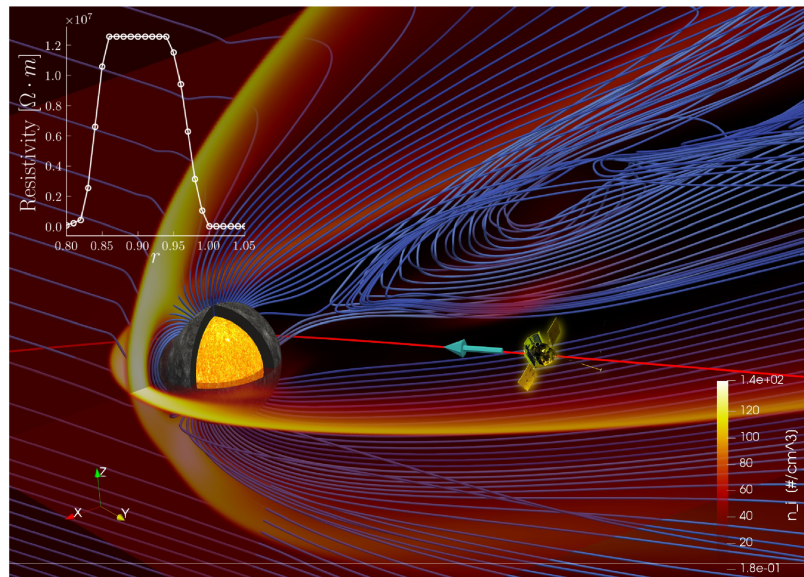


Figure 1. Top: Mercury's three-dimensional magnetosphere from the ten-moment multifluid calculation. The color contours depict the ion density in per cubic centimeter. The "hot" sphere inside Mercury represents its conducting core with a size of $R_c = 0.8 R_M$. The magnetic field lines are presented in blue. The red curve together with a cyan arrow represents MESSENGER's M2 trajectory. The radial resistivity profile adopted from Jia et al. (2015) is shown at the top-left corner. Bottom: Data-model comparison of magnetic fields along MESSENGER's M2 trajectory.

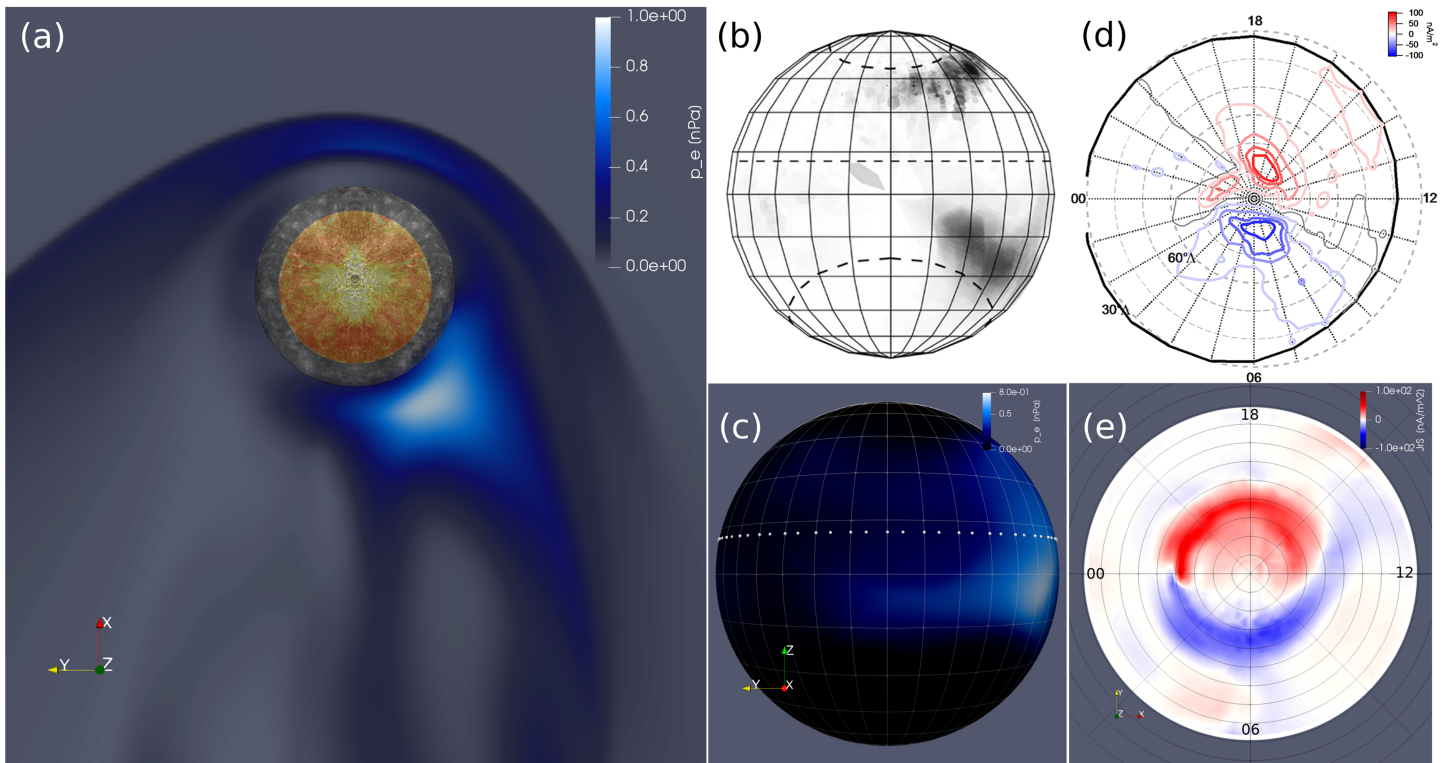


Figure 2. (a) Electron pressure (p_e) distribution in Mercury's magnetic equatorial plane at $z = 0.2R_M$. (b) X-ray spectrometer observations of energetic electron-induced surface fluorescence at Mercury's nightside surface from Lindsay et al. (2016). (c) Electron pressure (p_e) distribution at Mercury's nightside surface from the ten-moment model. (d) Contour plot of radial current density, $J_{r,S}$, at Mercury's (northern hemisphere) surface displayed versus local time in hours from Anderson et al. (2014) based on MESSENGER magnetometer observations. (e) Calculated radial current density, $J_{r,S}$, at Mercury's (northern hemisphere) surface from the ten-moment model.

Figure 1 (top) presents Mercury's three-dimensional magnetosphere from the ten-moment multifluid calculation. Magnetospheric characteristics such as the bow shock, magnetosheath, magnetopause, and magnetotail are clearly captured. In detail, the “hot” sphere ($0.8 R_M$) inside Mercury represents Mercury's electrically conductive core. M2 trajectory is plotted in red, pointing from nightside/duskside to dayside/dawnside and near Mercury's equatorial plane. Between the conducting core and planet's surface, there exists a highly resistive mantle. The radial resistivity profile shown in the top-left corner of Figure 1 has been adopted from Jia et al. (2015), and the white dots in the embedding plot are the grid points used in the model, that is, $0.01 R_M$.

To validate our model calculations, we compare the simulation results with MESSENGER's magnetic field data. Figures 1a–1d compare the model-calculated magnetic field components along M2 (in red) to MESSENGER magnetometer measurements (in black). Mercury's (unperturbed) intrinsic dipole magnetic field is also plotted as a reference (the blue dashed line in the last row) to illustrate how the global solar wind interaction affects Mercury's magnetosphere. Good agreement is observed between the model calculations and MESSENGER observations in Figure 1, thus ensuring the validity of our novel approach. Due to the lack of accurate solar wind measurements, we are not able to reproduce the flux transfer event (i.e., the spike structure at 08:50 UTC) observed by MESSENGER. As will be shown below, our model is capable of reproducing other important MESSENGER observations (beyond MHD approach); therefore, our numerical study by adopting this new model represents a crucial step toward establishing a modeling framework that enables self-consistent characterization of Mercury's tightly coupled interior-magnetosphere system.

3.2. Model Results Analysis and Discussion

3.2.1. Dawn-Dusk Asymmetries in Mercury's Magnetotail and Field-Aligned Currents

Dawn-dusk asymmetry is a ubiquitous phenomenon in planetary magnetotails. Notably, the ten-moment multifluid model is able to capture the remarkable asymmetry exhibited in Mercury's magnetotail current sheet. Figure 2a depicts the electron pressure scalar (p_e) in Mercury's magnetic equatorial plane (at $z =$

$0.2R_M$ in MSO), where the cross-tail current sheet is located. From Figure 2a, one can see that (1) more hot electrons are present at the dawnside especially in the inner tail region and (2) the asymmetry in p_e gradually decreases with increasing distance down the tail. By analyzing the simulation results, we find a slightly dawnward preference in magnetotail reconnection; however, the dawn-dusk asymmetry of the x -line is not significant, probably due to the lack of a dominant amount of Na^+ on the duskside as suggested by Poh et al. (2017). Here, we conclude that the exhibited asymmetry in hot electron distribution is caused by the dual effect of Mercury's magnetotail reconnection and the dawnward drifts of electrons. When approaching Mercury, the kinetic energy of the sunward reconnection outflow can be easily converted to thermal energy due to the tailward pressure gradient force, leading to a more notable asymmetry near the planet relative to the far tail. Meanwhile, the sunward electron flow also drifts to dawnside according to the perpendicular drift velocity of species s , $\mathbf{u}_{s\perp}$, derived from the cross-product of equation (2) and \mathbf{B} ,

$$\mathbf{u}_{s\perp} = \frac{\mathbf{E} \times \mathbf{B}}{B^2} - \frac{\nabla \cdot \mathbf{P}_s \times \mathbf{B}}{q_s n_s B^2} - \frac{m_s}{q_s B^2} \frac{d\mathbf{u}_s}{dt} \times \mathbf{B}, \quad (10)$$

where the first term is the $\mathbf{E} \times \mathbf{B}$ drift, the second term incorporates the diamagnetic drift and the curvature drift (given $\mathbf{P}_s = \mathbf{I}p_{s\perp} + \mathbf{bb}(p_{s\parallel} - p_{s\perp}) + \dot{\cdot}_s$, where $\dot{\cdot}_s$ is the off-diagonal part of the pressure tensor), while the last term contains the polarization drift. Interestingly, an asymmetry also manifests in the X-ray fluorescence from MESSENGER X-ray spectrometer observations at Mercury's nightside surface (Figure 2b). It is noteworthy that the calculated electron pressure, p_e , at Mercury's nightside surface (Figure 2c) depicts similar patterns as the X-ray fluorescence, supporting the idea of electron-induced surface fluorescence by Lindsay et al. (2016).

In addition to the asymmetries, we also present the simulation results for the field-aligned currents (or Birkeland currents) at Mercury's northern hemisphere surface in Figure 2e. The model predicts that the currents flow downward (in blue) at dawn and upward (in red) at dusk, which are consistent with MESSENGER observations shown in Figure 2d and analogous to Region 1 (R1) Birkeland currents at Earth. More importantly, our simulation results for the current density values at the planetary surface also agree well with MESSENGER observations. MESSENGER magnetic field data show that the maximum and minimum J_{RS} are $\pm 115 \text{ nA/m}^2$ (Anderson et al., 2014), and in comparison, the calculated maximum and minimum values from our model are 115 and -150 nA/m^2 , respectively.

3.2.2. Magnetotail and Magnetopause Reconnection

In order to demonstrate that the magnetic reconnection in our calculations is driven by detailed electron physics instead of numerical dissipation as in Jia et al. (2015, 2019), we further study the magnetic reconnection in Mercury's magnetotail and at the planet's magnetopause. We first investigate the magnetotail reconnection where the electron reconnection physics is less contaminated given that the tail is less affected by direct solar wind interaction than Mercury's dayside magnetopause. Note that previous full PIC simulations showed that the divergence of the off-diagonal elements of electron pressure tensor, P_e , is the main source of the reconnection electric field (Wang et al., 2015; Wilson et al., 2016), which can be verified from equation (9) as well. We therefore plot $P_{xy,e}$, $P_{xz,e}$, and $P_{yz,e}$ in the first row of Figure 3. Among the three P_e off-diagonal terms, $P_{yz,e}$ has the largest amplitude and gradient, therefore is the most important term, consistent with previous studies (e.g., Divin et al., 2016; Wang et al., 2018, 2015).

Subsequently, we investigated the magnetopause reconnection. Again the three P_e off-diagonal elements are shown in the second row of Figure 3, where the reconnection rate ranges from 0.08 to 0.2, depending on the locations. In comparison with Figures 3a–3c, Figures 3d–3f also exhibit different patterns for the P_e off-diagonal elements. In addition to the reconnection physics, Figure 3 clearly depicts the magnetopause location ($\approx 1.4 R_M$) and the bow shock location ($\approx 1.8 R_M$), consistent with the previous validated study by Jia et al. (2015).

3.2.3. Extreme Event Case Study

The solar wind parameters of M2 yield a dynamic pressure of $\approx 11 \text{ nPa}$, which is relatively weak for instigating a significant induction response from the conducting core. Thus, we followed the scenario in Jia et al. (2015) to investigate the core-induced induction response; the solar wind density and speed are deliberately enhanced to 80 cm^{-3} and 700 km/s , respectively, such that the solar wind dynamic pressure increases to $\approx 66 \text{ nPa}$, close to the pressure of 23 November 2011 event in Slavin et al. (2014). The ten-moment multifluid calculation of Mercury's magnetospheric response to this hypothetical extreme event is shown in

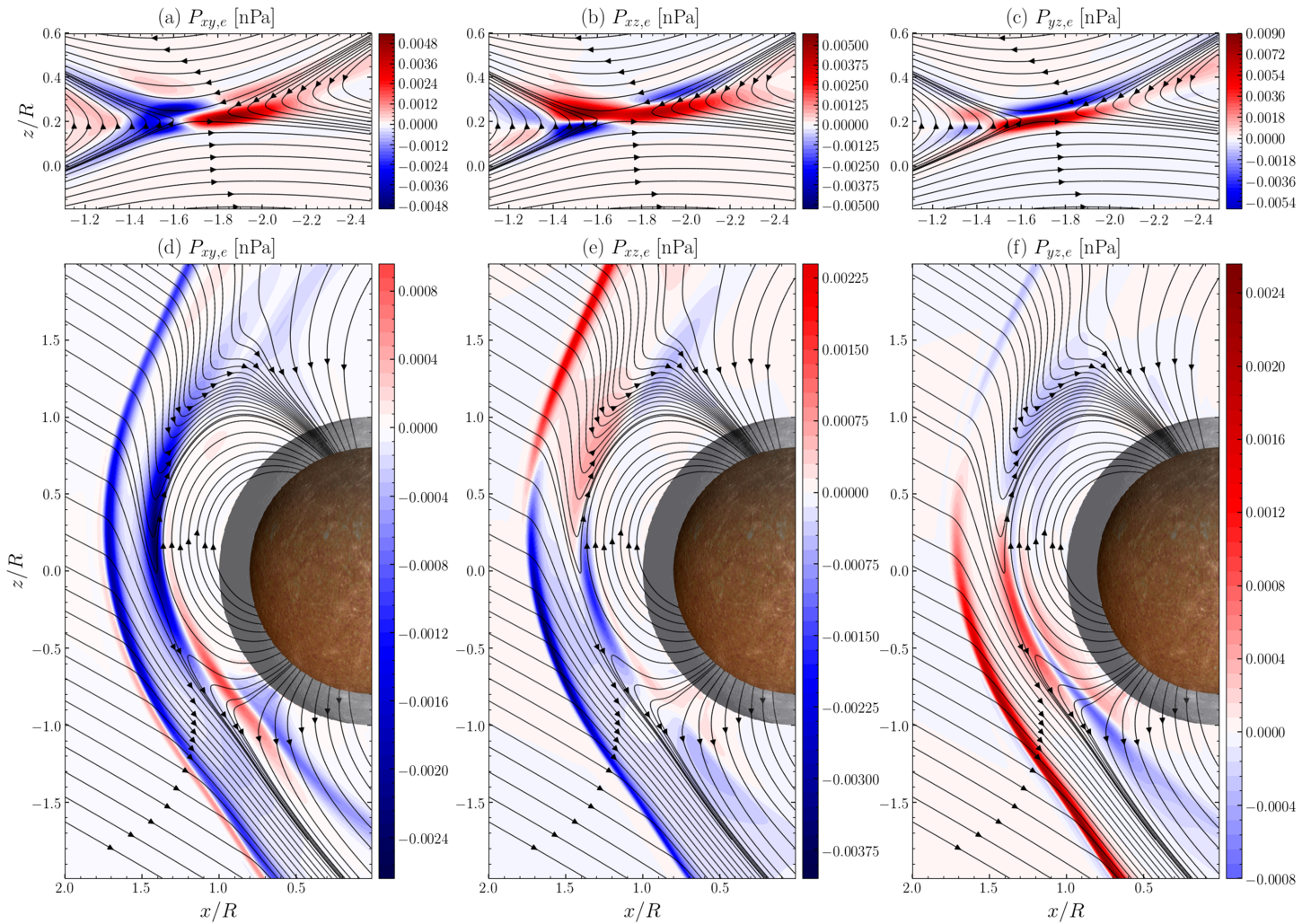


Figure 3. Magnetic reconnection in Mercury's magnetotail (first row) and at the magnetopause (second row). Different components of the electron pressure tensor off-diagonal terms ($P_{xy,e}$, $P_{xz,e}$, and $P_{yz,e}$ in nanopascal) are plotted.

Figure 4. From the middle panel, one can see that both the bow shock and magnetopause boundaries are compressed significantly. Compared with the M2 flyby, the new magnetopause standoff distance is compressed to $\approx 1.15R_M$, consistent with the results from Jia et al. (2015) for the same event study. In the bottom panel of Figure 4, we also compare the perturbation magnetic field B_{1z} between the normal solar wind case (of M2) and the extreme event. As expected, solar wind compression increases B_{1z} during the extreme event and squeeze the dayside magnetosphere. However, in order to demonstrate that the enhancement in B_{1z} is not purely a result of solar wind compression, we present the core surface current J_y for both cases, where the color contours on the core surface represent J_y intensity and the yellow curves with green arrows are the corresponding current streamlines. Following Faraday's law of induction, these currents generate additional magnetic flux that acts against the solar wind pressure. By adopting the same color scale, it is clear that J_y is much stronger in the extreme case than that in M2, indicating that the increase in B_{1z} is a result of both solar wind compression and induction responses. The enhanced B_{1z} and the intensified core surface current J_y clearly demonstrate the importance of the induction response during the extreme event.

In contrast to Jia et al. (2015), our calculations contain richer features. For the first time, our simulation illustrates the formation of plasmoids in Mercury's magnetotail through *collisionless* magnetic reconnection by including the reconnection electron physics. Plasmoids (or flux ropes) have, as a matter of fact, been observed by MESSENGER (DiBraccio et al., 2015). Theoretically speaking, these plasmoids are formed in

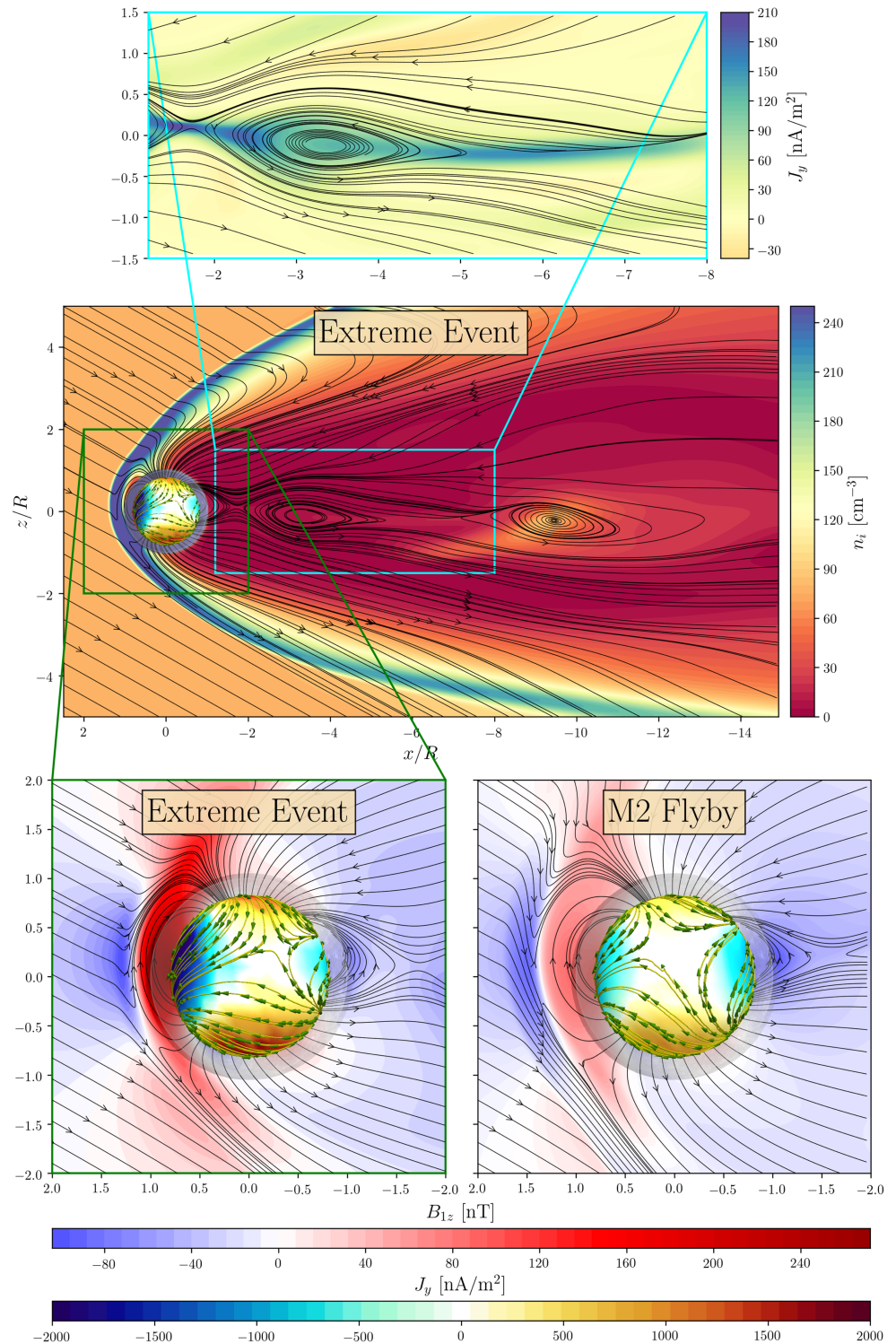


Figure 4. Mercury's magnetosphere in x - z (meridian) plane during a hypothetical extreme event. Plasmoids are formed in Mercury's magnetotail. The background color contours in the middle panel show the ion density in cubic centimeter. The lower left panel shows the zoomed-in subdomain where color contours in x - z plane represent the perturbation magnetic field B_{1z} (in nanotesla) and the color contours on the conducting core surface are the induction current J_y (in nanoamperes per square meter). Note that the streamlines of core surface currents are illustrated by the yellow curves with green arrows wrapping around the core. Compared with the lower right panel of M2, the B_{1z} and the induction current J_y from the extreme event are much stronger. The upper panel depicts the formation of a plasmoid within the cross-tail current sheet.

elongated and intense current sheets due to the plasmoid instability—an explosive instability resulting in the formation of plasmoids due to magnetic reconnection (e.g., Comisso et al., 2016). In order to demonstrate that plasmoids are indeed formed within the cross-tail current layer, we plot the current sheet density (J_y) together with the plasmoid in the top panel of Figure 4. These plasmoids are eventually transported either toward or away from the planet, and new plasmoids will repeatedly form within the cross-tail current sheet (not shown here), leading to the small but extremely dynamic magnetosphere of Mercury. The impact of extreme space weather events (such as coronal mass ejections given in, e.g., Slavin et al., 2014) on Mercury's dynamic magnetosphere will be investigated in detail in our future work.

4. Conclusion

For the first time, we utilize a three-dimensional ten-moment multifluid model to study solar wind interaction with Mercury from the planetary interior to its dynamic magnetosphere. Given the importance of the induction effects shown in the previous studies, we also include a highly resistive mantle and an electrically conductive iron core (of radius $0.8 R_M$) inside the planet body. Direct comparison between MESSENGER magnetometer data and model calculations show good agreement, strongly supporting the validity of this new model. The cross-tail current sheet asymmetry revealed by the model is also consistent with MESSENGER observations. We conclude that the exhibited asymmetry in hot electron distribution is caused by the dual effect of Mercury's magnetotail reconnection and the dawnward drifts of electrons. In addition, this model accurately reproduces the field-aligned currents measured by MESSENGER that cannot be captured by an MHD model. Our study of magnetotail and magnetopause reconnection shows that the off-diagonal elements of the electron pressure tensor, P_e , play a key role in *collisionless* magnetic reconnection. In order to investigate the induction effects, we have also studied Mercury's magnetospheric responses to a hypothetical extreme event. The simulation demonstrates that the induced magnetic fields help sustain a magnetopause, hindering the compression of the magnetopause down toward the surface. More interestingly, plasmoids (or flux ropes) are formed in Mercury's cross-tail current sheet, indicating Mercury's magnetotail being extremely dynamic.

Thanks to this novel fluid approach that incorporates detailed electron physics associated with, for example, *collisionless* magnetic reconnection and magnetic drifts, we are able to reproduce and interpret the observations beyond MHD. Here we want to reiterate the distinction between the multimoment multifluid approach and the (Hall) MHD approach from three perspectives. First, as mentioned earlier, the new model evolves the same set of equations (i.e., continuity, momentum, and pressure tensor equations) for both ions and electrons (without the quasi-neutral assumption) and updates the electric and magnetic fields by adopting the full Maxwell's equations. As a result, the new model incorporates the nonideal effects including the Hall effect, inertia, and tensorial pressures that are self-consistently embedded without the need for explicitly solving a generalized Ohm's law as MHD. Second, the new model supports all kinds of electromagnetic waves due to the inclusion of full Maxwell's equations. It is well-known that one of the shortcomings of Hall MHD lies in its failing to capture the right dispersion relation of Whistler waves (due to the assumption of massless electrons) when studying *collisionless* magnetic reconnection. Last but not the least, the new model contains an approximation to the Landau-fluid closure and therefore lower-order kinetic physics (Hammett & Perkins, 1990; Hunana et al., 2018; Wang et al., 2015). For instance, the novel fluid approach can correctly capture the lower hybrid drift instability, which can only be treated properly by a kinetic approach in the past (Ng et al., 2019).

In summary, MESSENGER furnished us with a great opportunity to study Mercury's dynamic magnetosphere. An abundance of useful data was returned from this mission, which stimulated numerous interesting studies. With the launch of the BepiColombo mission to Mercury in October 2018 (Benkhoff et al., 2010), Mercury's exploration will witness another notable surge after MESSENGER. A properly validated model that incorporates the electron physics essential for Mercury's *collisionless* magnetosphere will likely advance our understanding of the dynamic responses of Mercury's magnetosphere to global solar wind interactions. Hence, the three-dimensional global ten-moment multifluid model developed herein represents a crucial step toward establishing a revolutionary approach that enables the investigation of Mercury's tightly coupled interior-magnetosphere system beyond the traditional fluid model and has the potential to enhance the science returns of both the MESSENGER mission and the BepiColombo mission.

Acknowledgments

The authors thank Manasvi Lingam, Ryan Dewey, Suzanne Imber, Yuxi Chen, Yao Zhou, Chang Liu, and Y. Y. Lau for the helpful discussions and comments. This work was supported by NSF Grants AGS-0962698 and AGS-1338944, NASA Grants 80NSSC19K0621, NNH13AW511, and 80NSSC18K0288, and DOE Grant DE-SC0006670. The MESSENGER data used in this study are available from the PPI node of the Planetary Data System (<http://ppi.pds.nasa.gov>), and the model data were obtained from simulations using the GKEYLL framework developed at Princeton University, which is publicly available online (<https://bitbucket.org/ammahhakim/gkeyll>). Resources supporting this work were provided by the NASA High-End Computing (HEC) Program through the NASA Advanced Supercomputing (NAS) Division at Ames Research Center, the Titan supercomputer at the Oak Ridge Leadership Computing Facility at the Oak Ridge National Laboratory through the INCITE program, supported by the Office of Science of the U.S. Department of Energy under Contract DE-AC05-00OR22725, the National Energy Research Scientific Computing Center, a DOE Office of Science User Facility supported by the Office of Science of the U.S. Department of Energy under Contract DE-AC02-05CH11231, Cheyenne (doi:10.5065/D6RX99HX) provided by NCAR's CISL, sponsored by NSF, and Trilliant, a Cray XE6m-200 supercomputer at the UNH supported by the NSF MRI program under Grant PHY-1229408.

References

- Anderson, B. J., Johnson, C. L., Korth, H., Purucker, M. E., Winslow, R. M., Slavin, J. A., et al. (2011). The global magnetic field of mercury from MESSENGER orbital observations. *Science*, *333*, 1859. <https://doi.org/10.1126/science.1211001>
- Anderson, B. J., Johnson, C. L., Korth, H., Slavin, J. A., Winslow, R. M., Phillips, R. J., et al. (2014). Steady-state field-aligned currents at Mercury. *Geophysical Research Letters*, *41*, 7444–7452. <https://doi.org/10.1002/2014GL061677>
- Anderson, B. J., Johnson, C. L., Korth, H., Winslow, R. M., Borovsky, J. E., Purucker, v., et al. (2012). Low-degree structure in Mercury's planetary magnetic field. *Journal of Geophysical Research*, *117*, E00L12. <https://doi.org/10.1029/2012JE004159>
- Benkhoff, J., van Casteren, J., Hayakawa, H., Fujimoto, M., Laakso, H., Novara, M., et al. (2010). Bepicolombo—Comprehensive exploration of Mercury: Mission overview and science goals. *Planetary and Space Science*, *58*, 2–20. <https://doi.org/10.1016/j.pss.2009.09.020>
- Comisso, L., Lingam, M., Huang, Y.-M., & Bhattacharjee, A. (2016). General theory of the plasmoid instability. *Physics of Plasmas*, *100702*(10). <https://doi.org/10.1063/1.4964481>
- Dewey, R. M., Slavin, J. A., Raines, J. M., Baker, D. N., & Lawrence, D. J. (2017). Energetic electron acceleration and injection during dipolarization events in mercury's magnetotail. *Journal of Geophysical Research: Space Physics*, *122*, 12,170–12,188. <https://doi.org/10.1002/2017JA024617>
- DiBraccio, G. A., Slavin, J. A., Imber, S. M., Gershman, D. J., Raines, J. M., Jackman, C. M., et al. (2015). MESSENGER observations of flux ropes in Mercury's magnetotail. *Planetary and Space Science*, *115*, 77–89. <https://doi.org/10.1016/j.pss.2014.12.016>
- Dibraccio, G. A., Slavin, J. A., Boardsen, S. A., Anderson, B. J., Korth, H., Zurbuchen, T. H., et al. (2013). MESSENGER observations of magnetopause structure and dynamics at Mercury. *Journal of Geophysical Research: Space Physics*, *118*, 997–1008. <https://doi.org/10.1002/jgra.50123>
- Divin, A., Semenov, V., Korovinskiy, D., Markidis, S., Deca, J., Olshevsky, V., & Lapenta, G. (2016). A new model for the electron pressure nongyrotropy in the outer electron diffusion region. *Geophysical Research Letters*, *43*, 10,565–10,573. <https://doi.org/10.1002/2016GL070763>
- Dong, C., Bougher, S. W., Ma, Y., Lee, Y., Toth, G., Nagy, A. F., et al. (2018a). Solar wind interaction with the martian upper atmosphere: Roles of the cold thermosphere and hot oxygen corona. *Journal of Geophysical Research: Space Physics*, *123*, 6639–6654. <https://doi.org/10.1029/2018JA025543>
- Dong, C., Bougher, S. W., Ma, Y., Toth, G., Lee, Y., Nagy, A. F., et al. (2015). Solar wind interaction with the Martian upper atmosphere: Crustal field orientation, solar cycle, and seasonal variations. *Journal of Geophysical Research: Space Physics*, *120*, 7857–7872. <https://doi.org/10.1002/2015JA020990>
- Dong, C., Bougher, S. W., Ma, Y., Toth, G., Nagy, A. F., & Najib, D. (2014). Solar wind interaction with Mars upper atmosphere: Results from the one-way coupling between the multifluid MHD model and the MTGCM model. *Geophysical Research Letters*, *41*, 2708–2715. <https://doi.org/10.1002/2014GL059515>
- Dong, C., Huang, Z., & Lingam, M. (2019). Role of planetary obliquity in regulating atmospheric escape: G-dwarf versus M-dwarf Earth-like exoplanets. *The Astrophysical Journal Letters*, *882*, L16. <https://doi.org/10.3847/2041-8213/ab372c>
- Dong, C., Huang, Z., Lingam, M., Tóth, G., Gombosi, T., & Bhattacharjee, A. (2017b). The dehydration of water worlds via atmospheric losses. *The Astrophysical Journal*, *847*, L4. <https://doi.org/10.3847/2041-8213/aa8a60>
- Dong, C., Jin, M., Lingam, M., Airapetian, V. S., Ma, Y., & van der Holst, B. (2018c). Atmospheric escape from the TRAPPIST-1 planets and implications for habitability. *Proceedings of the National Academy of Sciences*, *115*, 260–265. <https://doi.org/10.1073/pnas.1708010115>
- Dong, C., Lee, Y., Ma, Y., Lingam, M., Bougher, S., Luhmann, J., et al. (2018b). Modeling Martian atmospheric losses over time: Implications for exoplanetary climate evolution and habitability. *The Astrophysical Journal Letters*, *859*, L14. <https://doi.org/10.3847/2041-8213/aac489>
- Dong, C., Lingam, M., Ma, Y., & Cohen, O. (2017a). Is Proxima Centauri b Habitable? A study of atmospheric loss. *The Astrophysical Journal*, *837*(2), L26. <https://doi.org/10.3847/2041-8213/aa6438>
- Dong, C., Wang, L., Bhattacharjee, A., Hakim, A., Huang, Y.-M., & Germaschewski, K. (2016). Magnetic reconnection in multispecies plasmas investigated by a kinetic fluid code. *In in APS Meeting Abstracts*. NO7.009.
- Exner, W., Heyner, D., Liuzzo, L., Motschmann, U., Shiota, D., Kusano, K., & Shibayama, T. (2018). Coronal mass ejection hits mercury: A.I.K.E.F. hybrid-code results compared to MESSENGER data. *Planetary and Space Science*, *153*, 89–99. <https://doi.org/10.1016/j.pss.2017.12.016>
- Gershman, D. J., Raines, J. M., Slavin, J. A., Zurbuchen, T. H., Sundberg, T., Boardsen, S. A., et al. (2015). MESSENGER observations of multiscale Kelvin-Helmholtz vortices at Mercury. *Journal of Geophysical Research: Space Physics*, *120*, 4354–4368. <https://doi.org/10.1002/2014JA020903>
- Grosser, J., Glassmeier, K.-H., & Stadelmann, A. (2004). Induced magnetic field effects at planet Mercury. *Planetary and Space Science*, *52*, 1251–1260. <https://doi.org/10.1016/j.pss.2004.08.005>
- Hakim, A. H. (2008). Extended mhd modelling with the ten-moment equations. *Journal of Fusion Energy*, *27*(1), 36–43. <https://doi.org/10.1007/s10894-007-9116-z>
- Hakim, A., Loverich, J., & Shumlak, U. (2006). A high resolution wave propagation scheme for ideal two-fluid plasma equations. *Journal of Computational Physics*, *219*, 418–442. <https://doi.org/10.1016/j.jcp.2006.03.036>
- Hammett, G. W., & Perkins, F. W. (1990). Fluid moment models for Landau damping with application to the ion-temperature-gradient instability. *Physical Review Letters*, *64*, 3019–3022. <https://doi.org/10.1103/PhysRevLett.64.3019>
- Hauck, S. A., Margot, J.-L., Solomon, S. C., Phillips, R. J., Johnson, C. L., Lemoine, F. G., et al. (2013). The curious case of Mercury's internal structure. *Journal of Geophysical Research: Planets*, *118*, 1204–1220. <https://doi.org/10.1002/jgre.20091>
- Heyner, D., Nabert, C., Liebert, E., & Glassmeier, K.-H. (2016). Concerning reconnection-induction balance at the magnetopause of Mercury. *Journal of Geophysical Research: Space Physics*, *121*, 2935–2961. <https://doi.org/10.1002/2015JA021484>
- Hood, L., & Schubert, G. (1979). Inhibition of solar wind impingement on Mercury by planetary induction currents. *Journal of Geophysical Research*, *84*, 2641–2647. <https://doi.org/10.1029/JA084iA06p02641>
- Hunana, P., Zank, G. P., Laurenza, M., Tenerani, A., Webb, G. M., Goldstein, M. L., et al. (2018). New closures for more precise modeling of landau damping in the fluid framework. *Physical Review Letters*, *121*(13), 135101. <https://doi.org/10.1103/PhysRevLett.121.135101>
- Imber, S. M., & Slavin, J. A. (2017). MESSENGER observations of magnetotail loading and unloading: Implications for substorms at mercury. *Journal of Geophysical Research: Space Physics*, *122*, 11,402–11,412. <https://doi.org/10.1002/2017JA024332>
- Jia, X., Slavin, J. A., Gombosi, T. I., Daldorff, L. K. S., Toth, G., & Holst, B. (2015). Global MHD simulations of Mercury's magnetosphere with coupled planetary interior: Induction effect of the planetary conducting core on the global interaction. *Journal of Geophysical Research: Space Physics*, *120*, 4763–4775. <https://doi.org/10.1002/2015JA021143>

- Jia, X., Slavin, J. A., Poh, G., DiBraccio, G. A., Toth, G., Chen, Y., et al. (2019). MESSENGER observations and global simulations of highly compressed magnetosphere events at Mercury. *Journal of Geophysical Research: Space Physics*, *124*, 229–247. <https://doi.org/10.1029/2018JA026166>
- Johansson, E. P. G., Mueller, J., & Motschmann, U. (2011). Interplanetary magnetic field orientation and the magnetospheres of close-in exoplanets. *Astronomy and Astrophysics*, *525*, A117. <https://doi.org/10.1051/0004-6361/201014802>
- Johnson, C. L., Philpott, L. C., Anderson, B. J., Korth, H., Hauck, S. A., Heyner, D., et al. (2016). MESSENGER observations of induced magnetic fields in Mercury's core. *Geophysical Research Letters*, *43*, 2436–2444. <https://doi.org/10.1002/2015GL067370>
- Kabin, K., Heimpel, M. H., Rankin, R., Aurnou, J. M., Gómez-Pérez, N., Paral, J., et al. (2008). Global MHD modeling of Mercury's magnetosphere with applications to the MESSENGER mission and dynamo theory. *Icarus*, *195*, 1–15. <https://doi.org/10.1016/j.icarus.2007.11.028>
- Kidder, A., Winglee, R. M., & Harnett, E. M. (2008). Erosion of the dayside magnetosphere at Mercury in association with ion outflows and flux rope generation. *Journal of Geophysical Research*, *113*, A09223. <https://doi.org/10.1029/2008JA013038>
- Ledvina, S. A., Brecht, S. H., Brain, D. A., & Jakosky, B. M. (2017). Ion escape rates from Mars: Results from hybrid simulations compared to MAVEN observations. *Journal of Geophysical Research: Space Physics*, *122*, 8391–8408. <https://doi.org/10.1002/2016JA023521>
- Liljeblat, E., Sundberg, T., Karlsson, T., & Kullen, A. (2014). Statistical investigation of Kelvin-Helmholtz waves at the magnetopause of Mercury. *Journal of Geophysical Research: Space Physics*, *119*, 9670–9683. <https://doi.org/10.1002/2014JA020614>
- Lindsay, S. T., James, M. K., Bunce, E. J., Imber, S. M., Korth, H., Martindale, A., & Yeoman, T. K. (2016). MESSENGER X-ray observations of magnetosphere-surface interaction on the nightside of Mercury. *Planetary and Space Science*, *125*, 72–79. <https://doi.org/10.1016/j.pss.2016.03.005>
- Lingam, M., Hirvijoki, E., Pfefferlé, D., Comisso, L., & Bhattacharjee, A. (2017). Nonlinear resistivity for magnetohydrodynamical models. *Physics of Plasmas*, *24*(4), 42120. <https://doi.org/10.1063/1.4980838>
- Ma, Y., Fang, X., Russell, C. T., Nagy, A. F., Toth, G., Luhmann, J. G., et al. (2014). Effects of crustal field rotation on the solar wind plasma interaction with Mars. *Geophysical Research Letters*, *41*, 6563–6569. <https://doi.org/10.1002/2014GL060785>
- Modolo, R., Hess, S., Mancini, M., Leblanc, F., Chaufray, J.-Y., Brain, D., et al. (2016). Mars-solar wind interaction: Lat hys, an improved parallel 3-D multispecies hybrid model. *Journal of Geophysical Research: Space Physics*, *121*, 6378–6399. <https://doi.org/10.1002/2015JA022324>
- Müller, J., Simon, S., Wang, Y.-C., Motschmann, U., Heyner, D., Schüle, J., et al. (2012). Origin of Mercury's double magnetopause: 3D hybrid simulation study with A.I.K.E.F. *Icarus*, *218*, 666–687. <https://doi.org/10.1016/j.icarus.2011.12.028>
- Ness, N. F., Behannon, K. W., Lepping, R. P., & Whang, Y. C. (1975). The magnetic field of Mercury. I. *Journal of Geophysical Research*, *80*, 2708–2716. <https://doi.org/10.1029/JA080i019p02708>
- Ness, N. F., Behannon, K. W., Lepping, R. P., Whang, Y. C., & Schatten, K. H. (1974). Magnetic field observations near mercury: Preliminary results from mariner 10. *Science*, *185*, 151–160. <https://doi.org/10.1126/science.185.4146.151>
- Ng, J., Hakim, A., & Bhattacharjee, A. (2018). Using the maximum entropy distribution to describe electrons in reconnecting current sheets. *Physics of Plasmas*, *25*(8), 82113. <https://doi.org/10.1063/1.5041758>
- Ng, J., Hakim, A., Bhattacharjee, A., Stanier, A., & Daughton, W. (2017). Simulations of anti-parallel reconnection using a nonlocal heat flux closure. *Physics of Plasmas*, *24*(8), 82112. <https://doi.org/10.1063/1.4993195>
- Ng, J., Hakim, A., Juno, J., & Bhattacharjee, A. (2019). Drift instabilities in thin current sheets using a two-fluid model with pressure tensor effects. *Journal of Geophysical Research: Space Physics*, *124*, 3331–3346. <https://doi.org/10.1029/2018JA026313>
- Ng, J., Huang, Y.-M., Hakim, A., Bhattacharjee, A., Stanier, A., Daughton, W., et al. (2015). The island coalescence problem: Scaling of reconnection in extended fluid models including higher-order moments. *Physics of Plasmas*, *22*(11), 112104. <https://doi.org/10.1063/1.4935302>
- Poh, G., Slavin, J. A., Jia, X., DiBraccio, G. A., Raines, J. M., Imber, S. M., et al. (2016). MESSENGER observations of cusp plasma filaments at Mercury. *Journal of Geophysical Research: Space Physics*, *121*, 8260–8285. <https://doi.org/10.1002/2016JA022552>
- Poh, G., Slavin, J. A., Jia, X., Raines, J. M., Imber, S. M., Sun, W.-J., et al. (2017). Coupling between Mercury and its nightside magnetosphere: Cross-tail current sheet asymmetry and substorm current wedge formation. *Journal of Geophysical Research: Space Physics*, *122*, 8419–8433. <https://doi.org/10.1002/2017JA024266>
- Richer, E., Modolo, R., Chanteur, G. M., Hess, S., & Leblanc, F. (2012). A global hybrid model for Mercury's interaction with the solar wind: Case study of the dipole representation. *Journal of Geophysical Research*, *117*, A10228. <https://doi.org/10.1029/2012JA017898>
- Slavin, J. A., Acuña, M. H., Anderson, B. J., Baker, D. N., Benna, M., Boardsen, S. A., et al. (2009). MESSENGER observations of magnetic reconnection in mercury's magnetosphere. *Science*, *324*, 606. <https://doi.org/10.1126/science.1172011>
- Slavin, J. A., DiBraccio, G. A., Gershman, D. J., Imber, S. M., Poh, G. K., Raines, J. M., et al. (2014). MESSENGER observations of Mercury's dayside magnetosphere under extreme solar wind conditions. *Journal of Geophysical Research: Space Physics*, *119*, 8087–8116. <https://doi.org/10.1002/2014JA020319>
- Slavin, J. A., Imber, S. M., Boardsen, S. A., DiBraccio, G. A., Sundberg, T., Sarantos, M., et al. (2012). MESSENGER observations of a flux-transfer-event shower at Mercury. *Journal of Geophysical Research*, *117*, A00M06. <https://doi.org/10.1029/2012JA017926>
- Slavin, J. A., Krimigis, S. M., Acuña, M. H., Anderson, B. J., Baker, D. N., Koehn, P. L., et al. (2007). MESSENGER: Exploring Mercury's magnetosphere. *Space Science Reviews*, *131*, 133–160. <https://doi.org/10.1007/s11214-007-9154-x>
- Slavin, J. A., Middleton, H. R., Raines, J. M., Jia, X., Zhong, J., Sun, W.-J., et al. (2019). Messenger observations of disappearing dayside magnetosphere events at Mercury. *Journal of Geophysical Research*, *124*, 6613–6635. <https://doi.org/10.1029/2019JA026892>
- Smith, D. E., Zuber, M. T., Phillips, R. J., Solomon, S. C., Hauck, S. A., Lemoine, F. G., et al. (2012). Gravity field and internal structure of mercury from MESSENGER. *Science*, *336*, 214. <https://doi.org/10.1126/science.1218809>
- Solomon, S. C., McNutt, R. L., Gold, R. E., & Domingue, D. L. (2007). MESSENGER mission overview. *Space Science Reviews*, *131*, 3–39. <https://doi.org/10.1007/s11214-007-9247-6>
- Sun, W.-J., Slavin, J. A., Fu, S., Raines, J. M., Sundberg, T., Zong, Q.-G., et al. (2015). MESSENGER observations of alfvénic and compressional waves during Mercury's substorms. *Geophysical Research Letters*, *42*, 6189–6198. <https://doi.org/10.1002/2015GL065452>
- Sundberg, T., Boardsen, S. A., Slavin, J. A., Blomberg, L. G., & Korth, H. (2010). The Kelvin-Helmholtz instability at Mercury: An assessment. *Planetary and Space Science*, *58*, 1434–1441. <https://doi.org/10.1016/j.pss.2010.06.008>
- Sundberg, T., Slavin, J. A., Boardsen, S. A., Anderson, B. J., Korth, H., Ho, G. C., et al. (2012). MESSENGER observations of dipolarization events in Mercury's magnetotail. *Journal of Geophysical Research*, *117*, A00M03. <https://doi.org/10.1029/2012JA017756>
- TenBarge, J., Ng, J., Juno, J., Wang, L., Hakim, A., & Bhattacharjee, A. (2019). An extended MHD study of the 16 October 2015 MMS diffusion region crossing. *Journal of Geophysical Research: Space Physics*, *124*. <https://doi.org/10.1029/2019JA026731>

- Tóth, G., Jia, X., Markidis, S., Peng, I. B., Chen, Y., Daldorff, L. K. S., et al. (2016). Extended magnetohydrodynamics with embedded particle-in-cell simulation of Ganymede's magnetosphere. *Journal of Geophysical Research: Space Physics*, *121*, 1273–1293. <https://doi.org/10.1002/2015JA021997>
- Trávníček, P. M., Schriver, D., Hellinger, P., Herčík, D., Anderson, B. J., Sarantos, M., & Slavin, J. A. (2010). Mercury's magnetosphere-solar wind interaction for northward and southward interplanetary magnetic field: Hybrid simulation results. *Icarus*, *209*, 11–22. <https://doi.org/10.1016/j.icarus.2010.01.008>
- Wang, L., Germaschewski, K., Hakim, A., Dong, C., Raeder, J., & Bhattacharjee, A. (2018). Electron physics in 3-D two-fluid 10-moment modeling of Ganymede's magnetosphere. *Journal of Geophysical Research: Space Physics*, *123*, 2815–2830. <https://doi.org/10.1002/2017JA024761>
- Wang, L., Hakim, A. H., Bhattacharjee, A., & Germaschewski, K. (2015). Comparison of multi-fluid moment models with particle-in-cell simulations of collisionless magnetic reconnection. *Physics of Plasmas*, *22*(1), 12108. <https://doi.org/10.1063/1.4906063>
- Wang, L., Hakim, A., Ng, J., Dong, C., & Germaschewski, K. (2019). Exact and locally implicit source term solvers for multifluid-Maxwell systems. *arXiv e-prints*, *arXiv:1909.04125*.
- Wilson, F., Neukirch, T., Hesse, M., Harrison, M. G., & Stark, C. R. (2016). Particle-in-cell simulations of collisionless magnetic reconnection with a non-uniform guide field. *Physics of Plasmas*, *23*(3), 32302. <https://doi.org/10.1063/1.4942939>
- Winslow, R. M., Anderson, B. J., Johnson, C. L., Slavin, J. A., Korth, H., Purucker, M. E., et al. (2013). Mercury's magnetopause and bow shock from MESSENGER magnetometer observations. *Journal of Geophysical Research: Space Physics*, *118*, 2213–2227. <https://doi.org/10.1002/jgra.50237>
- Zhong, J., Wan, W. X., Wei, Y., Slavin, J. A., Raines, J. M., Rong, Z. J., et al. (2015). Compressibility of Mercury's dayside magnetosphere. *Geophysical Research Letters*, *42*, 10,135–10,139. <https://doi.org/10.1002/2015GL067063>
- Zweibel, E. G., & Yamada, M. (2009). Magnetic reconnection in astrophysical and laboratory plasmas. *Annual Review of Astronomy and Astrophysics*, *47*, 291–332. <https://doi.org/10.1146/annurev-astro-082708-101726>